Direct observation of terahertz topological valley transport

YU-LIANG HONG,[1,3] GONG-HUI TANG,[1,3] RU-WEN PENG,[1,4] (iD)
REN-HAO FAN,[1,5] (iD) ZHONG-LI MA,[1] ZHENG WANG,[1] YUE JIANG,[1]
LE-DI CHEN,[1] AND MU WANG[1,2,6]

[1]*National Laboratory of Solid State Microstructures, School of Physics, and Collaborative Innovation Center of Advanced Microstructures, Nanjing University, Nanjing 210093, China*
[2]*American Physical Society, Ridge, NY 11961, USA*
[3]*These two authors contributed equally*
[4]*rwpeng@nju.edu.cn*
[5]*rhfan@nju.edu.cn*
[6]*muwang@nju.edu.cn*

Abstract: Topological photonics offers the possibility of robust transport and efficiency enhancement of information processing. Terahertz (THz) devices, such as waveguides and beam splitters, are prone to reflection loss owing to their sensitivity to defects and lack of robustness against sharp corners. Thus, it is a challenge to reduce backscattering loss at THz frequencies. In this work, we constructed THz photonic topological insulators and experimentally demonstrated robust, topologically protected valley transport in THz photonic crystals. The THz valley photonic crystal (VPC) was composed of metallic cylinders situated in a triangular lattice. By tuning the relevant location of metallic cylinders in the unit cell, mirror symmetry was broken, and the degenerated states were lifted at the K and K' valleys in the band structure. Consequently, a bandgap of THz VPC was opened, and a nontrivial band structure was created. Based on the calculated band structure, THz field distributions, and valley Berry curvature, we verified the topological phase transition in such type of THz photonic crystals. Further, we showed the emergence of valley-polarized topological edge states between the topologically distinct VPCs. The angle-resolved transmittance measurements identified the bulk bandgap in the band structure of the VPC. The measured time-domain spectra demonstrated the topological transport of valley edge states between distinct VPCs and their robustness against bending and defects. Furthermore, experiments conducted on a topological multi-channel intersectional device revealed the valley-polarized characteristic of the topological edge states. This work provides a unique approach to reduce backscattering loss at the THz regime. It also demonstrates potential high-efficiency THz functional devices such as topologically protected beam splitters, low-loss waveguides, and robust delay lines.

1. Introduction

The topological phases of matter have been extensively studied in recent decades due to their unique boundary states and transport properties. Enlightened by the generality of the topological band theory of electrons in solid-state systems [1], photonics systems with similar band structures have provided an ideal platform to investigate the topological effects, giving rise to the rapidly growing field of topological photonics. As an extension of topological insulators from condensed matter physics to optics, photonic topological insulators (PTIs), have been proposed and experimentally investigated from different approaches, such as photonic analogous to the quantum Hall effect [2–7], quantum spin Hall effect [8–15], and quantum valley Hall effect [16–19]. As a unique feature, topological edge states enable topologically protected light transport, which is robust against sharp corners and fabricating imperfections, and allow unidirectional transport that can

inhibit back reflection [4,12,13,20–24]. Up to now, PTIs have demonstrated substantial potential in novel optical devices, such as reflectionless waveguides [4], robust delay lines [20], and topological lasers [25–27].

The valley, a discrete degree of freedom (DOF) in condensed matter physics, refers to a pair of degenerated but inequivalent states of the Brillouin zone, *i.e.*, the K and K' points. It was first proposed in two-dimensional (2D) hexagonal crystals such as graphene and transition metal dichalcogenides [28–31]. Those materials exhibit nontrivial Berry curvature in the K and K' valleys of the band structure, which gives rise to a valley-dependent topological index. As a new type of information carrier, valley DOF of photons also demonstrates potential applications in valley-based information encoding and processing [32,33]. Breaking inversion symmetry has been shown to induce a nontrivial valley Hall phase that generates opposite Berry curvatures in K and K' valleys in the momentum space [16,34]. To date, valley Hall PTIs and the resultant edge states have been proposed and demonstrated in all-dielectric photonic crystals [16,24], plasmonic crystals [35–38], and on-chip integrated devices [39,40].

Most experiments on the PTIs have been carried out in the microwave [4,13,18,21,22] and optical frequencies [8,25–27], and the relevant researches are very limited at the terahertz (THz) regime. The THz waves fall between infrared waves and microwaves in the electromagnetic spectrum [41,42], which possess a large available bandwidth [43]. They are of considerable importance for applications in communications technologies [44–48], biological and medical sciences [49–51], homeland security [42,52–54], and space exploration [55–58]. However, the lack of proper materials and technology makes it challenging to fabricate efficient THz devices [59]. Applying the robust topological transport to THz systems would strongly encourage the development of practical and robust devices for THz systems. For instance, due to the lack of a high-power THz laser, an electrically THz quantum cascade laser based on topologically protected valley edge states has been demonstrated. The valley edge states circulate around the cavity without experiencing localization [60]. Recently, the effect of asymmetry on topological edge states and relevant transmissions in an all-dielectric THz photonic crystal has been explored [61,62], which might be particularly useful in 6G communications. In addition, robust THz topological valley transport on the all-silicon chip has been realized to reduce the loss in communication networks, and it enables real-time transmission of uncompressed 4K high-definition video [40]. And topological THz planar air-channel metallic waveguides for communications are also implemented by two-dimensional printing and gold-sputtering [15]. However, due to the complex design and difficult fabrication, the mass production of complex THz devices seems formidable.

Here, we use a more straightforward structure to realize a two-dimensional (2D) valley photonic crystal (VPC) at THz regime, which is composed of the triangular lattice arrangement of low-cost metallic steel wires. It is shown that by tuning the relevant location of metallic steel wires in the unit cell to break the mirror symmetry, the degenerated states at the K and K' valleys were lifted, creating a bandgap and producing a nontrivial band structure. Using a finite-element method to quantify the band structure, the electromagnetic field distribution and valley Berry curvature at the K and K' valleys, we showed the topological phase transition in such types of THz photonic crystals. Further, we demonstrated the emergence of valley-polarized topological edge states between topologically distinct VPCs. Then we fabricated the THz samples, and directly measured the transmittances of THz wave propagation along with differently-shaped interfaces, such as a straight topological interface, a bending topological interface, and a topological interface with the disorder. We confirmed the robustness of the one-way broadband topological transport and the suppression of the backscattering of various types of defects at the interfaces between two VPCs with different valley phases. Additionally, the results obtained from the experiments conducted using the topological multi-channel intersectional device demonstrated the valley-polarized characteristic of the edge states. The experimental results were in agreement with the simulations.

2. THz VPC design and topological phase transitions

The designed THz photonic crystal consisted of metal cylinders arranged in a triangular lattice. If we do not consider the propagation of light along the z-direction, the entire structure can be considered two-dimensional, as depicted in Fig. 1(a). The unit cell contained three identical metal cylinders with a diameter of $d = 250$ μm; the distance between the nearest columns was set as $t = 300$ μm, and the lattice constant was $a = 750$ μm. Here, we primarily focused on transverse-electric modes in which the E_z component vanishes. Based on Maxwell's equations, the wave equation for THz transport in such a photonic crystal can be derived as

$$\nabla \times (\frac{1}{\varepsilon(\boldsymbol{r})} \nabla \times H_z(\boldsymbol{r})) = (\frac{\omega}{c})^2 H_z(\boldsymbol{r}), \tag{1}$$

where $H_z(\boldsymbol{r})$ is the out-of-plane magnetic field, $\varepsilon(\boldsymbol{r})$ is the position-dependent electric permittivity, ω is the frequency, and c is the speed of light in the vacuum. The first Brillouin zone (FBZ) of the triangular lattice is shown in the bottom-right part of Fig. 1(a). The calculations on the photonic band structures of THz photonic crystals were carried out using a commercial software package (COMSOL Multiphysics), and periodic boundary conditions were applied to the system. The materials of the photonic crystals were assumed to be perfect electric conductors within the targeted THz frequency range.

By varying the relevant location of metallic cylinders in the unit cell, the photonic band structure of the THz photonic crystal can be tuned. As shown in Fig. 1(a), a rotation angle (θ) of metal cylinder location is defined as the angle between one of principal axes of the unit cell and the x-axis, which characterized the relevant location of metallic cylinders in a unit cell and provided a flexible and steady control of the bandgap gradually by breaking the in-plane mirror symmetry. A structure with the C_3 symmetry has a period of $2\pi/3$. In particular, in the case of mirror symmetry in the x-direction, the photonic crystal possesses a pair of degenerate Dirac points at the K and K' valleys at 0.212 THz because of the C_{3v} symmetry in the momentum space, as shown in Fig. 1(b). When varying the rotation angle, the C_{3v} symmetry can be broken, which lifted the degeneracy at the K and K' valleys and resulted in the formation of a bandgap. Here, we focused on two cases: $\theta = 30°$ (VPC1) and $\theta = -30°$ (VPC2). We calculated the band structures for VPC1 and VPC2, respectively. Because VPC2 is the mirror-symmetry partner of VPC1, both VPC1 and VPC2 have the same band structure, as seen in Fig. 1(b). The simulated H_z phase profiles at the K valley are presented in Fig. 1(c) for both two VPCs. For the two lowest bands, there were two eigenstates with either left circularly polarized (LCP) light or right circularly polarized (RCP) light. Although VPC1 and VPC2 possessed the same band structure, the corresponding frequencies of the LCP (RCP) light were reversed at the same valley (as shown in Fig. 1(c)), indicating a topological phase transition.

To understand the evolution of the topological phase, we explored the eigenfrequencies of the LCP (RCP) states at K valley as a function of the rotation angle θ in different photonic crystals (to see Fig. 1(d)). As the rotation angle increased from $\theta = 0$ to $\theta = 30°$, the frequencies of the LCP states increased gradually, whereas the frequencies of the RCP states decreased. Alternatively, the frequency changes of the K' valley chiral states were opposite. The state exchange with opposite chirality occurred at $\theta = 0$ or $\theta = \pm 60°$, where the mirror symmetry resumed. Once the mirror symmetry was broken, the degenerate states were lifted, resulting in a bandgap. Around the degenerate points, the LCP and RCP states sequence was inverted, signifying a topological phase transition.

Next, we tried to show different topologies in VPC1 and VPC2 from the point of view of Berry curvature. Based on the Hamiltonian in the system [16–18] $\hat{H}_{K/K'} = v_D \sigma_x \delta k_x + \sigma_y \delta k_y + v_D \Delta_p \sigma_z$, the local Berry curvature of the first band at the K/K' valley can be analytically calculated by $\Omega_{K/K'} = \pm \frac{\Delta_p}{2(\delta k^2 + \Delta_p{}^2)^{3/2}}$. Here, v_D is the group velocity, $\delta \boldsymbol{k} = \boldsymbol{k} - \boldsymbol{k}_{K/K'}$ is the reciprocal vector with respect to the K/K' point, σ_i ($i = x, y, z$) denotes the Pauli matrices, and Δ_p is proportional
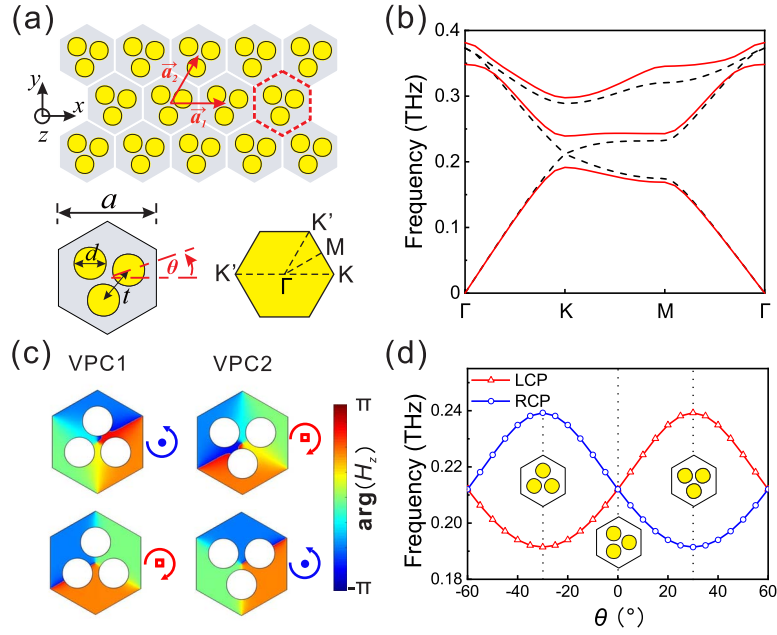
Fig. 1. The THz photonic crystal and its bulk band diagram. (a) Schematic of the THz photonic crystal, which was composed of metal cylinders. The red dashed line denotes a unit cell. The diameter of the cylinder was $d = 250$ μm, the distance between adjacent cylinders was $t = 300$ μm, and the lattice constant was $a = 750$ μm. The rotation angle θ of metal cylinder location is the angle between one of principal axes of the unit cell and the x-axis. (b) Bulk band structure of the photonic crystals with $\theta = 0°$ (black dashed line), and $\theta = \pm30°$ (solid red line). (c) Phase profiles at the K valley of the two lowest bulk bands for VPC1 ($\theta = 30°$) and VPC2 ($\theta = -30°$). The color scale shows z-oriented magnetic field H_z, and the blue and red arrows respectively denote LCP and RCP states. (d) Calculated eigenfrequencies of LCP (red curve) and RCP (blue curve) states at the K valley when θ varied.

to the bandwidth of bandgap. In order to consolidate the analytical results, we numerically calculated the distribution of the Berry curvature of the first band in the FBZ and confirmed the valley Hall topological phase in these two THz photonic crystals. Figure 2(a) showed that non-zero Berry curvatures of both VPC1 and VPC2 were primarily localized near the K or K' valley. In the case of VPC1, the Berry curvature was opposite in sign for the K and K' valleys, *i.e.*, a peak at K while a dip at K' (left panel in Fig. 2(a)). On the contrary, VPC2 reversed the Berry curvature distribution of K and K' valleys (right panel in Fig. 2(a)). Then the valley Chern numbers can be derived by

$$C_{K/K'} = \frac{1}{2\pi} \int_{HBZ_{K/K'}} \Omega(\mathbf{k}) d^2 k, \tag{2}$$

where $\Omega(\mathbf{k})$ is the Berry curvature, and the integration is carried over half of the FBZ surrounding the K or K' valley [16]. We had $C_K = 1/2$ and $C_{K'} = -1/2$ for VPC1, and $C_K = -1/2$ and $C_{K'} = 1/2$ for VPC2. The signs of valley Chern numbers for VPC1 and VPC2 were opposite at the same type of valley, indicating different nontrivial topologies in VPC1 and VPC2. Anyway, it should also be noted that due to the time-reversal symmetry, the global integration of the Berry curvature over the FBZ was zero in both VPC1 and VPC2.
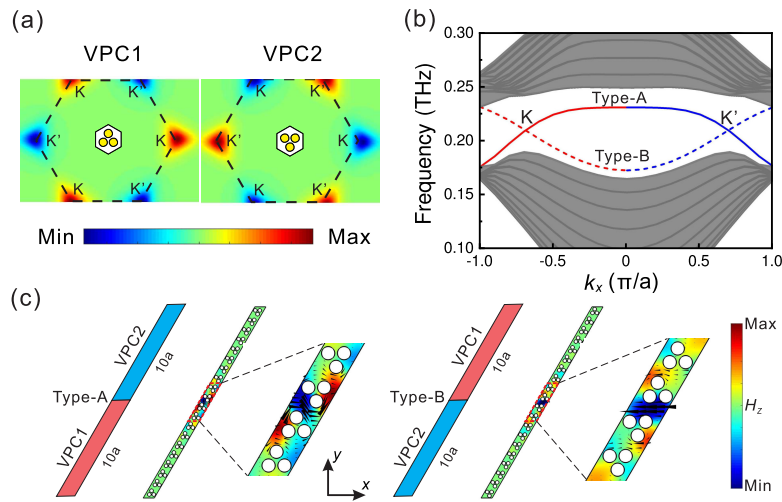
Fig. 2. Topologically protected edge waves with different valley polarization. (a) Distribution of Berry curvature of VPC1 (left panel) and distribution of Berry curvature of VPC2 (right panel). (b) Dispersion relation for the ribbon-shaped supercell comprising 20 unit cells with domain walls in the center. The shaded regions represent the projected bulk dispersions, and the solid/dashed lines represent Type-A/Type-B interfaces. (c) Schematics of supercells with different interfaces. The magnified area shows the intensity distribution of $|H_z|$ near the interface at the K valley and the Poynting power flow denoted by the black arrows.

In the case of the valley Hall effect, the non-zero valley Chern numbers denoted a nontrivial intrinsic topology, thus indicating the presence of robust edge states at the interface between two topologically distinct VPCs. The bulk-boundary corresponding principle ensured the emergence of edge states under the condition of a difference in valley Chern numbers ($|C_V| = |C_K - C_{K'}| = 1$) across the interface. Thus, we constructed a ribbon-shaped supercell comprising 20 unit cells with domain walls in the center; Fig. 2(c) shows the simulated band structure. Here, Type-A refers to the structure with VPC1 in the lower half and VPC2 in the upper half. In contrast, the opposite configuration is referred to as Type-B. As expected, the band structure of the ribbon-shaped VPC with supercells revealed the presence of two edge states that intersected each other at the K and K' valleys (Fig. 2(b)). It can be seen that the group velocity for both Type-A and Type-B interfaces at K and K' valleys was opposite. Additionally, we found that the intensity distribution $|H_z|$ was confined to the area near the interface and that the corresponding Poynting vectors (black arrows) for the two different interfaces at the K valley shown in the insets in Fig. 2(c) were consistent with the directions of the group velocity, as predicted. This is a manifestation of valley-chirality of the valley Hall effect, which can be summarized as follows: the valley-polarized edge states were locked in one propagating direction in the absence of inter-valley scattering.

3. Experimental demonstration of valley edge states and robust topological transport

To experimentally demonstrate the topological valley transport in the VPCs and the valley edge states between topologically distinct VPCs, we fabricated three types of THz VPC samples: VPC1, VPC2, and various assembly of VPC1 and VPC2. Steel wires with the diameter $d = 250$ μm used as cylinders were arranged in the requirements of lattices in VPC1, VPC2, and their assembly, respectively. It is worth to mention that the diameter of cylinders should be within the appropriate range to guarantee a large bandgap and photonic crystal modes. Here, for the

convenience of experimental measurements (a larger bandgap around 0.2 THz), we choose $d = 250$ μm. To maintain the shape of lattice stable, a metal plate with the thickness of 50 μm was attached at ends of cylinders, in which the holes with the diameter of 250 μm was also etched. The photograph of an assembled sample was shown in Fig. 3(b), which used two metal plates with lattice shown in Fig. 3(a). The measurements were carried out using a THz real-time spectrometer (EKSPLA/THz, Lithuania), as schematically shown in Fig. 3(c). The linearly polarized THz waves along y direction went through a metal waveguide which was applied to enhance the THz signal intensity and optical collimation, and then coupled into the VPC sample from the left end of the topological interface. After passing through the VPC sample, the propagating waves were collected by detector as shown in Fig. 3(d). By comparing the measured transmission spectrum intensity of each sample to the reference spectrum, we obtained their transmittance spectra.
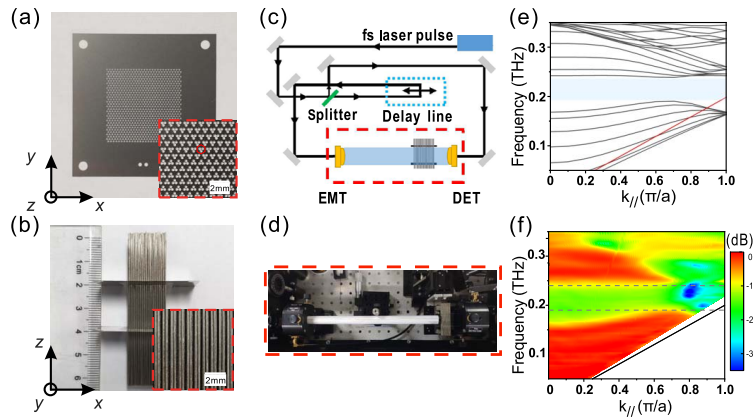
Fig. 3. Transmission measurements for THz VPCs. (a) Photograph of a fabricated sample, where the inset is a magnification to show the detailed structure. (b) Assembled experimental sample, where the inset is a partial enlargement of the sample. (c) Experimental setup used to perform transmittance measurements. (d) The magnified photograph corresponds to the red dotted frame in (c). (e) Calculated dispersion relation for the bulk VPC1 sample along with $k_{//}$; the light-blue shadowed region corresponds to the bulk bandgap, and the red line are artificially labeled light cone. (f) Measured dispersion map for VPC1, the gray dotted area represents the bulk bandgap, and the black line represents the light cone.

The fabricated samples VPC1 and VPC2 were characterized by the angle-resolved transmittance measurements to identify bulk band dispersions. Considering that a VPC1 sample comprised 4 periodicities along the x-axis (total length 3.0 mm) and 32 periodicities along the y-axis (total width 20.8 mm or so), we let the incident THz wave propagate along the x-axis, through the sample VPC1. Then we rotated the sample in the x-y plane along the z-axis so as to change the incident angle α, thus causing the momentum component along the interface tangential component to continuously vary. Our experiments measured the transmittances when the incident angle α varied from 0°. to 66°. These angle-resolved transmittances were further merged into the dispersion map, using the relation between the in-plane vector $k_{//}$ and incident angle α as $k_{//} = 2\pi \sin\alpha / \lambda$ (Here λ is the wavelength of the incident THz wave). Figure 3(f) shows the measured dispersion map, where the bulk band was branched, and the bandgap was clearly observed between 0.19–0.24 THz. This observation is consistent with the calculated photonic band structure of the VPC1 sample, in which we use periodic conditions in both x and y directions (as shown in Fig. 3(e)), based on the COMSOL Multiphysics platform. The difference between the experimental data and numerically calculated results was minimal, which was likely attributable to the imprecise operations of the measurement process. Due to thgeometric symmetry between

VPC1 and VPC2, VPC2 can be obtained by rotating 180° of VPC1 along the *z*-axis. The measured dispersion map of VPC2 is almost consistent with the result of VPC1. Here, we demonstrated the existence of a bulk bandgap in VPC1 and VPC2.

The fascinating property of valley Hall topologically protected edge states is that they are robust against defects without inter-valley scattering. To demonstrate robust topological transport, we employed a Type-A structure waveguide channel consisting of VPC1 and VPC2; the VPC1 was placed on top of the VPC2, and they both comprised 20 unit cells along the *x*-axis and 10 unit cells along the *y*-axis, as shown in Fig. 4(a). A line light source was placed to the left of the edge waveguide channel; it was set to operate at 0.21 THz to excite the edge states; we also applied the scattering boundary condition in the outer region to avoid the reflection of THz wave. The intensity distribution results for $|H_z|$ clearly show that the THz waves could propagate along the edge of the waveguide channel (along the *x*-axis) without any significant scattering. Furthermore, the THz wave was localized near the channel and did not diffuse to the VPC1 or VPC2 region; this indicates that the bulk region was insulating. In addition, the following two different types of defects were introduced under the premise of the preceding straight waveguide channel: (1) the structure units were selected and replaced at random near the interface, consequently introducing disorder (Fig. 4(b)); and (2) the interface was transformed into a Ω-shaped channel with 120° turns (Fig. 4(c)). By introducing the THz wave at the same position as previously mentioned, we found the simulated magnetic field distributions (Fig. 4(b) and 4(c)) confirmed that the THz wave propagates smoothly along the interface; notably, there was no backscattering, despite the existence of the disorder and bending.
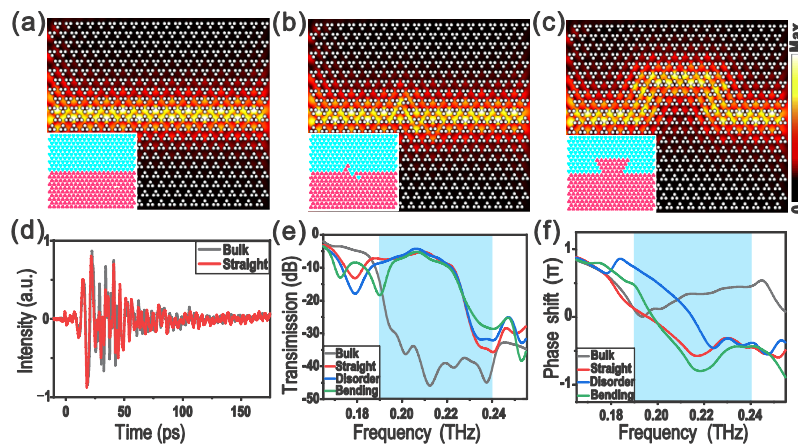
Fig. 4. Simulated and experimental results for the evaluation of topological transport robustness. (a)–(c) Simulated intensity distribution results for $|H_z|$ field at 0.21 THz for a straight interface (a), disordered interface (b), and bending interface (c); each inset shows a top view of each of the three topologically distinct interfaces. (d) Measured time-domain spectra for THz radiation transmitted through a straight interface (red curve) and through the bulk, which did not contain an interface (black curve). (e) Measured transmittance results for the four different interface conditions, i.e., the straight interface (red curve), disordered interface (blue curve), bending interface (green curve), and no interface (black curve). (f) The phase shift results were measured for the four different configurations with respect to waves that were freely propagating through air.

To experimentally demonstrate the robust topological transport, we performed transmittance measurements on three different waveguide channels, with either side of which containing 20×10 unit cells. Firstly, we measured the time-domain signal, $\boldsymbol{E}(t)$, of the THz pulse transmitted through a sample with a straight interface waveguide channel shown in Fig. 4(d) as an example,

and it transmitted through the above bulk sample VPC1 (without any interface) for comparison. Then, from the measured time-domain signals, we obtained the measured transmittances of four VPCs, as shown in Fig. 4(e). The light-blue shadowed region corresponds to the bulk bandgap, which ranged from 0.19-0.24 THz. The low transmittance (approximately −40 dB) of the bulk sample VPC1 without the waveguide channel indicated the presence of a bandgap. On the contrary, the relatively high transmittances (approximately −10 dB) of the samples with an interface waveguide channel revealed the presence of edge states. The transmittances of all three differently shaped interfaces were very similar, and the transmission through each of these interfaces was relatively high within the bandgap. Thereafter, we can find the transmission efficiency through each interface was nearly unaffected by the defects. Although there exists the loss in the sample, which mainly comes from the mode mismatch between the sources and the topological interfaces (the intrinsic loss of metal in THz regime is very limited), the observations are also in good agreement with the simulated results. The measured phase shifts of the transmitted THz waves with respect to that of the freely-propagating THz waves in the air were shown in Fig. 4(f). The extent of the phase shifts induced by the edge states decreased when the incident wave frequency increased; conversely, the phase shifts of the bulk state varied relatively smoothly. The phase shift trends of the disordered interface and bending interface were similar to those of the straight interface. All of the measured transmittance results and phase shift results reveal the intrinsic robustness of the topological edge states against disorder and bending.

4. Observation of topological valley-polarized transport in THz multi-channel VPCs

We designed a topological multi-channel intersectional device to show the robustness of the topological transport of the valley-polarized edge states. Figure 5(a) illustrated that this device consisted of three Type-A shaped interfaces and a Type-B shaped interface; it also included an input port and three output ports labeled as Port 1, 2, and 3. According to the results of theoretical analysis, the propagating direction of the edge states is dependent on the valley-polarized characteristic; in Fig. 5(a), the black and green arrows respectively indicate K and K' valley-polarized edge states. These edge modes with Type-A and Type-B configurations were not coupled in forward propagating because of differences in the valley-polarized characteristics. Thus, if the valley was conserved at the intersection point, the incident THz wave was expected to follow the path toward Port 1 or 3, but not Port 2. Indeed, the simulated results for the intensity distribution of $|H_z|$ confirmed this hypothesis (Fig. 5(b)).

We fabricated this topological multi-channel intersectional device with a similar fabrication approach, and the geometrical parameters were the same as that described in Sec.3. The THz waves were input at the center of the outer-left end, and the transmittances were measured at the output Port 1, Port 2, and Port 3, respectively. The measured time-domain signal and transmittance spectral results for the three output ports are illustrated in Fig. 5(c) and Fig. 5(d), respectively. From Fig. 5(d), one may find that the signal measured at Port 1 and 3 was consistently higher than that measured at Port 2, although there was slight signal intensity at Port 2 due to the scattering. These results support the idea that the forward propagation of THz wave at multi-channel intersections is related to the interface type, or, more accurately speaking, is strongly dependent of the valley-polarized characteristic of edge states. This feature can be exploited in the design of a novel topologically protected THz beam splitter.
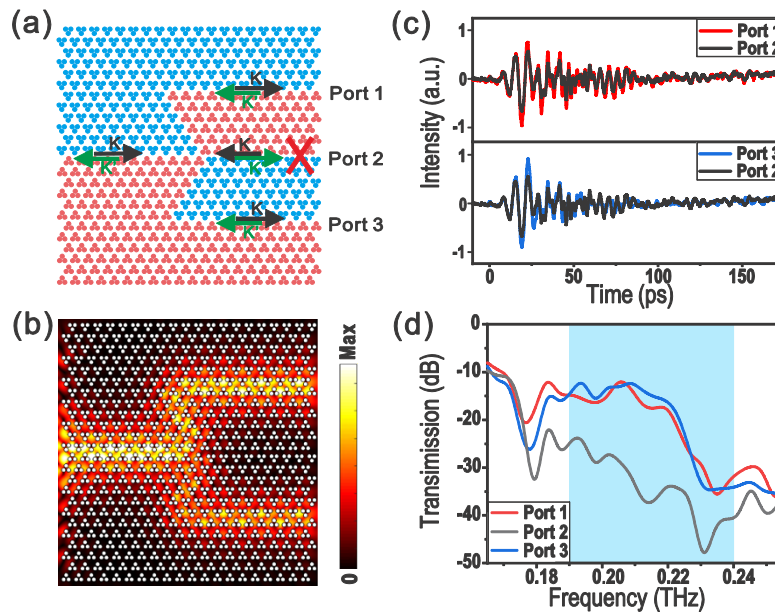
Fig. 5. Simulated and experimental topological results for the valley-dependent edge states. (a) Schematic of the topological multi-channel intersections; the black and green arrows respectively denote the direction of THz wave propagation at the K and K' valleys. (b) The simulated intensity distribution of $|H_z|$ field. (c) The measured time-domain spectral results for THz radiation transmission by different ports; the red, black, and blue curves respectively correspond to the time-domain spectra measured from Port 1, 2, and 3. (d) The measured transmittance from Port 1, 2, and 3; the blue shaded region denotes the bulk bandgap.

5. Conclusions

This article theoretically and experimentally demonstrated THz topological valley transport in metallic photonic crystals composed of metallic cylinders arranged in a triangular lattice. The calculated band structure, valley Chern numbers, and field distributions of THz waves confirmed the topological phase transition in the THz photonic crystals. Further, it demonstrated the emergence of valley-polarized topological edge states between topologically distinct VPCs. The experimental measurements on the angle-resolved transmittance showed that the bulk bandgap indeed existed in the band structure of VPC. The experiments also demonstrated the topological transport of valley edge states between two distinct VPCs and their robustness against both bending and defects. Moreover, the experiments confirmed the multi-channel THz topological propagation of the valley-polarized edge states and their valley-dependent transport. Our studies indicate that the implementation of valley Hall photonic insulators is straightforward and beneficial at the THz frequency range. Especially, the THz topological insulator can exploit the broadband benefit, and THz transmission of their valley edge states dramatically reduces backscattering loss. We prospect that the VPCs may have potential applications in high-efficiency transmission devices for THz waves as low-loss waveguides, topological beam splitters, robust delay lines, and logical gate devices.

Disclosures. The authors declare no conflicts of interest.

Data availability. Data underlying the results presented in this paper are not publicly available at this time but may be obtained from the authors upon reasonable request.

References

1. A. Bansil, H. Lin, and T. Das, "Colloquium: Topological band theory," Rev. Mod. Phys. **88**(2), 021004 (2016).
2. F. D. M. Haldane and S. Raghu, "Possible realization of directional optical waveguides in photonic crystals with broken time-reversal symmetry," Phys. Rev. Lett. **100**(1), 013904 (2008).
3. S. Raghu and F. D. M. Haldane, "Analogs of quantum-Hall-effect edge states in photonic crystals," Phys. Rev. A **78**(3), 033834 (2008).
4. Z. Wang, Y. Chong, J. D. Joannopoulos, and M. Soljačić, "Observation of unidirectional backscattering-immune topological electromagnetic states," Nature **461**(7265), 772–775 (2009).
5. Z. Wang, Y. D. Chong, J. D. Joannopoulos, and M. Soljačić, "Reflection-free one-way edge modes in a gyromagnetic photonic crystal," Phys. Rev. Lett. **100**(1), 013905 (2008).
6. Y. Poo, R.-x. Wu, Z. Lin, Y. Yang, and C. T. Chan, "Experimental Realization of Self-Guiding Unidirectional Electromagnetic Edge States," Phys. Rev. Lett. **106**(9), 093903 (2011).
7. J. W. You, Z. Lan, and N. C. Panoiu, "Four-wave mixing of topological edge plasmons in graphene metasurfaces," Sci. Adv. **6**(13), eaaz3910 (2020).
8. M. Hafezi, S. Mittal, J. Fan, A. Migdall, and J. M. Taylor, "Imaging topological edge states in silicon photonics," Nat. Photonics **7**(12), 1001–1005 (2013).
9. L. Lu, J. D. Joannopoulos, and M. Soljačić, "Topological photonics," Nat. Photonics **8**(11), 821–829 (2014).
10. C. He, X.-C. Sun, X.-P. Liu, M.-H. Lu, Y. Chen, L. Feng, and Y.-F. Chen, "Photonic topological insulator with broken time-reversal symmetry," Proc. Natl. Acad. Sci. U. S. A. **113**(18), 4924–4928 (2016).
11. L. H. Wu and X. Hu, "Scheme for Achieving a Topological Photonic Crystal by Using Dielectric Material," Phys. Rev. Lett. **114**(22), 223901 (2015).
12. Y. Yang, Y. F. Xu, T. Xu, H. X. Wang, J. H. Jiang, X. Hu, and Z. H. Hang, "Visualization of a Unidirectional Electromagnetic Waveguide Using Topological Photonic Crystals Made of Dielectric Materials," Phys. Rev. Lett. **120**(21), 217401 (2018).
13. S. Yves, R. Fleury, T. Berthelot, M. Fink, F. Lemoult, and G. Lerosey, "Crystalline metamaterials for topological properties at subwavelength scales," Nat. Commun. **8**(1), 16023 (2017).
14. H. Xiong, Q. Wu, Y. Lu, R. Wang, Q. Zhang, J. Qi, J. Yao, and J. Xu, "Polarization-resolved edge states in terahertz topological photonic crystal," Opt. Express **27**(16), 22819–22826 (2019).
15. M. T. A. Khan, H. Li, N. N. M. Duong, A. Blanco-Redondo, and S. Atakaramians, "3D-Printed Terahertz Topological Waveguides," Adv. Mater. Technol. **6**(7), 2100252 (2021).
16. T. Ma and G. Shvets, "All-Si valley-Hall photonic topological insulator," New J. Phys. **18**(2), 025012 (2016).
17. X.-D. Chen, F.-L. Zhao, M. Chen, and J.-W. Dong, "Valley-contrasting physics in all-dielectric photonic crystals: Orbital angular momentum and topological propagation," Phys. Rev. B **96**(2), 020202 (2017).
18. X. Wu, Y. Meng, J. Tian, Y. Huang, H. Xiang, D. Han, and W. Wen, "Direct observation of valley-polarized topological edge states in designer surface plasmon crystals," Nat. Commun. **8**(1), 1304 (2017).
19. Y. Kang, X. Ni, X. Cheng, A. B. Khanikaev, and A. Z. Genack, "Pseudo-spin-valley coupled edge states in a photonic topological insulator," Nat. Commun. **9**(1), 3029 (2018).
20. M. Hafezi, E. A. Demler, M. D. Lukin, and J. M. Taylor, "Robust optical delay lines with topological protection," Nat. Phys. **7**(11), 907–912 (2011).
21. F. Gao, Z. Gao, X. Shi, Z. Yang, X. Lin, H. Xu, J. D. Joannopoulos, M. Soljačić, H. Chen, L. Lu, Y. Chong, and B. Zhang, "Probing topological protection using a designer surface plasmon structure," Nat. Commun. **7**(1), 11619 (2016).
22. X. Cheng, C. Jouvaud, X. Ni, S. H. Mousavi, A. Z. Genack, and A. B. Khanikaev, "Robust reconfigurable electromagnetic pathways within a photonic topological insulator," Nat. Mater. **15**(5), 542–548 (2016).
23. K. Lai, T. Ma, X. Bo, S. Anlage, and G. Shvets, "Experimental realization of a reflections-free compact delay line based on a photonic topological insulator," Sci. Rep. **6**, 28453 (2016).
24. X.-D. Chen, F.-L. Shi, H. Liu, J.-C. Lu, W.-M. Deng, J.-Y. Dai, Q. Cheng, and J.-W. Dong, "Tunable electromagnetic flow control in valley photonic crystal waveguides," Phys. Rev. Appl. **10**(4), 044002 (2018).
25. B. Bahari, A. Ndao, F. Vallini, A. El Amili, Y. Fainman, and B. Kanté, "Nonreciprocal lasing in topological cavities of arbitrary geometries," Science **358**(6363), 636–640 (2017).
26. M. A. Bandres, S. Wittek, G. Harari, M. Parto, J. Ren, M. Segev, D. N. Christodoulides, and M. Khajavikhan, "Topological insulator laser: Experiments," Science **359**(6381), eaar4005 (2018).
27. Y. Ota, R. Katsumi, K. Watanabe, S. Iwamoto, and Y. Arakawa, "Topological photonic crystal nanocavity laser," Commun. Phys. **1**(1), 86 (2018).
28. Y. Zhang, T.-T. Tang, C. Girit, Z. Hao, M. C. Martin, A. Zettl, M. F. Crommie, Y. R. Shen, and F. Wang, "Direct observation of a widely tunable bandgap in bilayer graphene," Nature **459**(7248), 820–823 (2009).
29. K. F. Mak, K. L. McGill, J. Park, and P. L. McEuen, "The valley Hall effect in MoS_2 transistors," Science **344**(6191), 1489–1492 (2014).
30. G. Aivazian, Z. Gong, A. M. Jones, R.-L. Chu, J. Yan, D. G. Mandrus, C. Zhang, D. Cobden, W. Yao, and X. Xu, "Magnetic control of valley pseudospin in monolayer WSe_2," Nat. Phys. **11**(2), 148–152 (2015).

31. L. Ju, Z. Shi, N. Nair, Y. Lv, C. Jin, J. Velasco, C. Ojeda-Aristizabal, H. A. Bechtel, M. C. Martin, A. Zettl, J. Analytis, and F. Wang, "Topological valley transport at bilayer graphene domain walls," Nature **520**(7549), 650–655 (2015).
32. G. Wu, N.-Y. Lue, and L. Chang, "Graphene quantum dots for valley-based quantum computing: A feasibility study," Phys. Rev. B **84**(19), 195463 (2011).
33. N. Rohling and G. Burkard, "Universal quantum computing with spin and valley states," New J. Phys. **14**(8), 083008 (2012).
34. J.-W. Dong, X.-D. Chen, H. Zhu, Y. Wang, and X. Zhang, "Valley photonic crystals for control of spin and topology," Nat. Mater. **16**(3), 298–302 (2017).
35. M. Jung, Z. Fan, and G. Shvets, "Midinfrared plasmonic valleytronics in metagate-tuned graphene," Phys. Rev. Lett. **121**(8), 086807 (2018).
36. P. Qiu, R. Liang, W. Qiu, H. Chen, J. Ren, Z. Lin, J.-X. Wang, Q. Kan, and J.-Q. Pan, "Topologically protected edge states in graphene plasmonic crystals," Opt. Express **25**(19), 22587–22594 (2017).
37. J. W. You, Z. Lan, Q. Bao, and N. C. Panoiu, "Valley-Hall topological plasmons in a graphene nanohole plasmonic crystal waveguide," IEEE J. Sel. Top. Quantum Electron. **26**(6), 1–8 (2020).
38. Y. Wang, J. Wei You, Z. Lan, and N. C. Panoiu, "Topological valley plasmon transport in bilayer graphene metasurfaces for sensing applications," Opt. Lett. **45**(11), 3151–3154 (2020).
39. X. T. He, E. T. Liang, J. J. Yuan, H. Y. Qiu, X. D. Chen, F. L. Zhao, and J. W. Dong, "A silicon-on-insulator slab for topological valley transport," Nat. Commun. **10**(1), 872 (2019).
40. Y. Yang, Y. Yamagami, X. Yu, P. Pitchappa, J. Webber, B. Zhang, M. Fujita, T. Nagatsuma, and R. Singh, "Terahertz topological photonics for on-chip communication," Nat. Photonics **14**(7), 446–451 (2020).
41. M. Tonouchi, "Cutting-edge terahertz technology," Nat. Photonics **1**(2), 97–105 (2007).
42. B. Ferguson and X.-C. Zhang, "Materials for terahertz science and technology," Nat. Mater. **1**(1), 26–33 (2002).
43. R. H. Fan, B. Xiong, R. W. Peng, and M. Wang, "Constructing metastructures with broadband electromagnetic functionality," Adv. Mater. **32**(27), 1904646 (2020).
44. J. Federici and L. Moeller, "Review of terahertz and subterahertz wireless communications," J. Appl. Phys. **107**(11), 111101 (2010).
45. T. Kleine-Ostmann and T. Nagatsuma, "A review on terahertz communications research," J. Infrared, Millimeter, Terahertz Waves **32**(2), 143–171 (2011).
46. T. Nagatsuma, G. Ducournau, and C. C. Renaud, "Advances in terahertz communications accelerated by photonics," Nat. Photonics **10**(6), 371–379 (2016).
47. R. H. Fan, Y. Zhou, X. P. Ren, R. W. Peng, S. C. Jiang, D. H. Xu, X. Xiong, X. R. Huang, and M. Wang, "Freely tunable broadband polarization rotator for terahertz waves," Adv. Mater. **27**(7), 1201–1206 (2015).
48. S. Liu, T. J. Cui, Q. Xu, D. Bao, L. Du, X. Wan, W. X. Tang, C. Ouyang, X. Y. Zhou, H. Yuan, H. F. Ma, W. X. Jiang, J. Han, W. Zhang, and Q. Cheng, "Anisotropic coding metamaterials and their powerful manipulation of differently polarized terahertz waves," Light: Sci. Appl. **5**(5), e16076 (2016).
49. S. W. Smye, J. M. Chamberlain, A. J. Fitzgerald, and E. Berry, "The interaction between terahertz radiation and biological tissue," Phys. Med. Biol. **46**(9), R101–R112 (2001).
50. R. M. Woodward, B. E. Cole, V. P. Wallace, R. J. Pye, D. D. Arnone, E. H. Linfield, and M. Pepper, "Terahertz pulse imaging in reflection geometry of human skin cancer and skin tissue," Phys. Med. Biol. **47**(21), 3853–3863 (2002).
51. D. F. Plusquellic, K. Siegrist, E. J. Heilweil, and O. Esenturk, "Applications of terahertz spectroscopy in biosystems," ChemPhysChem **8**(17), 2412–2431 (2007).
52. D. L. Woolard, E. R. Brown, M. Pepper, and M. Kemp, "Terahertz frequency sensing and imaging: A time of reckoning future applications," Proc. IEEE **93**(10), 1722–1743 (2005).
53. W. L. Chan, J. Deibel, and D. M. Mittleman, "Imaging with terahertz radiation," Rep. Prog. Phys. **70**(8), 1325–1379 (2007).
54. D. Liu, Y.-L. Hong, R.-H. Fan, H. Jing, R.-W. Peng, Y. Lai, X.-R. Huang, C. Sun, and M. Wang, "Bendable disordered metamaterials for broadband terahertz invisibility," Opt. Express **28**(3), 3552–3560 (2020).
55. P. Kaufmann, J.-P. Raulin, C. G. Giménez De Castro, H. Levato, D. E. Gary, J. E. R. Costa, A. Marun, P. Pereyra, A. V. R. Silva, and E. Correia, "A new solar burst spectral component emitting only in the terahertz range," Astrophys. J. **603**(2), L121–L124 (2004).
56. R. K. Melugin and H.-P. Roeser, *Airborne Telescope Systems II* (SPIE, 2003).
57. P. H. Siegel, "THz instruments for space," IEEE Trans. Antennas Propag. **55**(11), 2957–2965 (2007).
58. J. Wei, D. Olaya, B. S. Karasik, S. V. Pereverzev, A. V. Sergeev, and M. E. Gershenson, "Ultrasensitive hot-electron nanobolometers for terahertz astrophysics," Nat. Nanotechnol. **3**(8), 496–500 (2008).
59. S. Atakaramians, S. Afshar, T. M. Monro, and D. Abbott, "Terahertz dielectric waveguides," Adv. Opt. Photonics **5**(2), 169–215 (2013).
60. Y. Zeng, U. Chattopadhyay, B. Zhu, B. Qiang, J. Li, Y. Jin, L. Li, A. G. Davies, E. H. Linfield, B. Zhang, Y. Chong, and Q. J. Wang, "Electrically pumped topological laser with valley edge modes," Nature **578**(7794), 246–250 (2020).
61. K. M. Devi, S. Jana, and D. R. Chowdhury, "Topological edge states in an all-dielectric terahertz photonic crystal," Opt. Mater. Express **11**(8), 2445–2458 (2021).
62. S. Jana, K. M. Devi, and D. R. Chowdhury, "Effect of asymmetry on terahertz transmissions in topological photonic crystals comprising of dielectric rod structures," Opt. Commun. **505**, 127589 (2022).